International Journal of Multiphase Flow 64 (2014) 44–54

Contents lists available at ScienceDirect

International Journal of Multiphase Flow

journal homepage: www.elsevier.com/locate/ijmulflow

Toward numerical modeling of fine particle suspension using a two-way coupled Euler–Euler model: Part 2: Simulation of particle-induced Rayleigh–Taylor instability

Yi-Ju Chou [a,*], Fu-Chun Wu [b], Wu-Rong Shih [b]

[a] Institute of Applied Mechanics, National Taiwan University, Taipei 106, Taiwan
[b] Department of Bioenvironmental Systems Engineering, National Taiwan University, Taipei 106, Taiwan

ARTICLE INFO

Article history:
Received 3 June 2013
Received in revised form 18 December 2013
Accepted 19 December 2013
Available online 10 January 2014

Keywords:
Sediment suspension
Euler–Euler model
Rayleigh–Taylor instability

ABSTRACT

In the present study, we develop a three-dimensional two-way coupled Euler–Euler model to simulate the dilute suspensions of fine particles. In addition to the inter-phase drag term, commonly appearing in standard EE formulations, the model formulation includes inter-phase momentum exchange resulting from added mass, which is not negligible in solid–liquid systems. Moreover, through a two-phase pressure projection method, the present numerical model ensures that the incompressibility of the solid–liquid mixture is also taken into consideration. A series of numerical experiments on the particle-induced Rayleigh–Taylor (RT) instability is carried out to investigate bulk mixing attributable to the initial concentration of particles, covering a range of suspension from dilute to dense ($O(0.001 - 0.05)$ in volume fraction). This study identifies deviations in the current two-phase simulations by comparing them with single-phase approximations. Our results indicate that the deviations are caused by non-equilibrium particle inertia and mixture incompressibility. In the dilute suspension, it is found that the non-equilibrium particle inertia enhances vertical motion of bubbles and spikes, resulting in a higher efficiency in vertical mixing, compared to the results from single-phase simulations. However, as initial concentration increases, the influence of mixture incompressibility becomes more pronounced and is able to induce a significant suppression of upward-moving motion of bubbles, which in turn decreases the efficiency of vertical mixing.

1. Introduction

The suspension of fine sediment is an important geophysical phenomenon with critical implications in geological sciences as well as in countless engineering practices. Recent advances in computational power have made numerical simulation an important tool in the study of suspended sediment. Strategies for the numerical simulation of small-scale processes are generally categorized into two types. The first type employs three-dimensional turbulence-resolving flow solvers, most of which employ direct numerical simulation (DNS), capable of revealing the details of turbulent features in particle-laden turbulent flows. For example, DNS has been used to study the dynamics of underwater turbidity currents, with particular a focus on interactions between turbulence and particle-induced stratification (e.g. Necker et al., 2002, 2006, 2009a,b, 2012). These studies apply single-phase approximation to particles under the assumptions of equilibrium state and scalar-limit (zero volume) conditions. As a result, this approach is applicable only under conditions of the very dilute suspension, which are easily violated in realistic flow problems. The second category involves the utilization of the Euler–Euler (EE) two phase model, which treats the sediment phase as a continuum. The EE approach takes non-equilibrium particle inertia into account, thereby modeling sediment transport in a more precise manner to a wider range of concentrations (Balachandar and Eaton, 2010). This approach has recently been applied to the study of suspension problems in unidirectional open channels flows (e.g. Greimann and Holly, 2001, 2003a, 2010, 2011) as well as oscillatory flows (e.g. Hsu et al., 2003b,a, 2005). These studies simplify the governing equations to one- or two-dimensional equations in conjunction with the $k - \epsilon$ equations for turbulence closure. These are employed mainly for analysis, rather than resolving details of flow features. A modified EE modeling approach is presented in Cantero et al. (2008), in which the result derived in Ferry and Balachandar (2001) is employed to reformulate an EE model to study turbidity currents in two-dimensional settings. The model accounts for non-equilibrium particle inertia while retaining the computational efficiency of the single-phase method. However, without considering feedback of non-equilibrium particle inertia to the carrier flow

* Corresponding author. Tel.: +886 2 33665068.
E-mail address: yjchou@iam.ntu.edu.tw (Y.-J. Chou).

0301-9322/$ - see front matter © 2014 Elsevier Ltd. All rights reserved.
http://dx.doi.org/10.1016/j.ijmultiphaseflow.2013.12.009

and volumes occupied by particles, the model by Cantero et al. (2008) only applies to dilute suspensions.

Under the assumptions of small particle size and low concentration, Chou et al. (2013) present a two-way coupled Euler–Euler (EE) formulation to describe the motions of two-phase flow comprising suspended fine particles and liquid. The former assumption enables the use of Stokes drag to represent the only inter-phase momentum exchange that depends on the local velocity difference between two phases. This is a standard approach used in the study of dispersed two-phase flow systems. The second assumption is that the effect of inter-particle stresses due to particle collision and friction are negligible. In the present study, the formulation is discretized using the finite-volume method, to develop a three-dimensional numerical model capable of capturing important features of two-phase particle-laden turbulence for fine suspension problems. In addition to considering Stokes drag, as in the standard framework of EE modeling, the proposed numerical model takes added mass into account and ensures the incompressibility of the solid–liquid mixture. The numerical model is then employed to study the Rayleigh–Taylor (RT) instability driven by inertia particles.

The RT instability occurs at the interface vertically separating a high-density fluid (top) and a low-density fluid (bottom), at which the perturbation grows in a self-similar manner to form a mixing layer between two fluids with different densities. During the growth of the mixing layer, the low density (ρ_l) fluid penetrates into the high density (ρ_h) fluid as bubbles while the high density fluid penetrates into the low density fluid to form spikes. The moving speed of the bubbles and spikes as well as the entrainment from the ambient fluid (in the miscible case) are responsible for the bulk mixing of the reversed stratified flow. A well-known relationship describing the evolution of the thickness (h) of the mixing layer is written as (Read, 1984; Youngs, 1984; Linden et al., 1994; Young et al., 2001; Dimonte et al., 2004)

$$h = \alpha A g t^2, \tag{1}$$

where $A = (\rho_u - \rho_l)/(\rho_u + \rho_l)$ is the Atwood number and α is a constant coefficient. One important focus of previous studies has been the value of α, which is an important parameter indicating the bulk mixing. This depends on the dynamics of bubbles and spikes as well as the experimental setting. A comprehensive survey of experimental data suggests that α lies within the range between 0.04 and 0.08 with a mean of about 0.057 (Dimonte et al., 2004). In the context of sediment suspension, high-density fluids can result from the presence of fine sediment in the water column, which commonly forms in the river upstream through erosion. When the energetic discharge of sediment-containing riverine flow encounters a relatively still and clear water body without strong background stratification, the particle-induced RT instability can occur, leading to large-scale vertical convection. The resulting convective velocity is far greater than the settling velocity calculated using the Stokes' law for individual particles. This is a dominant sedimentation process found in lakes, reservoirs, and estuaries (Bradley, 1965). The RT instability has been extensively studied for immiscible and miscible cases using both numerical and experimental methods (see Dimonte et al., 2004 for a comprehensive literature survey). Studies on the particle-induced RT instability have been focused on the experimental observation (Hoyal et al., 1999; Maxworthy, 1999; Parsons et al., 2001) and theoretical analysis (Burns and Meiburg, 2012), and numerical studies have yet to be conducted. This study performs a series of three-dimensional numerical simulations of the particle-induced RT instability to investigate flow features and bulk mixing behavior. Through a comparison to the single-phase approximation, we aim to address the influence of non-equilibrium particle inertia and mixture incompressibility in bulk mixing, particle accumulation, and flow energetics.

The rest of the paper is organized as follows. In Section 2, we briefly review the proposed mathematical formulation and numerical method is presented. In Section 3, the domain setting and simulation parameters are presented. In Section 4, we summarize two-phase effects derived in the theoretical framework. Simulation results are discussed in Section 5, and conclusions are provided in Section 6.

2. Mathematical formulation and numerical model

Under the assumptions of small particle size and low concentration, Chou et al. (2013) presented a two-way coupled momentum equations of the Euler–Euler (EE) formulation as follows:

$$\begin{aligned}\frac{\partial}{\partial t}\begin{bmatrix}\overline{\mathbf{u}}_d\\ \overline{\mathbf{u}}_c\end{bmatrix} + \begin{bmatrix}\overline{\mathbf{u}}_d\cdot\nabla\overline{\mathbf{u}}_d\\ \overline{\mathbf{u}}_c\cdot\nabla\overline{\mathbf{u}}_c\end{bmatrix} &= \mathcal{A}\begin{bmatrix}\frac{\overline{\mathbf{u}}_c-\overline{\mathbf{u}}_d}{\tau_p}\\ -\frac{\phi}{1-\phi}s\frac{\overline{\mathbf{u}}_c-\overline{\mathbf{u}}_d}{\tau_p}\end{bmatrix} + \mathcal{A}\begin{bmatrix}\frac{s-1}{s}\mathbf{g}\\ 0\end{bmatrix} + \mathcal{A}\begin{bmatrix}-\frac{\nabla\overline{p}}{s}\\ -\nabla\overline{p}\end{bmatrix}\\ &+ \begin{bmatrix}\frac{\phi}{1-\phi}\mathcal{A}_{(1,2)}\nu\nabla^2\overline{\mathbf{u}}_d\\ \mathcal{A}_{(2,2)}\nu\nabla^2\overline{\mathbf{u}}_c\end{bmatrix} + \begin{bmatrix}\mathcal{A}_{(1,2)}\nu\nabla^2\overline{\mathbf{u}}_c\\ \frac{\phi}{1-\phi}\mathcal{A}_{(2,2)}\nu\nabla^2\overline{\mathbf{u}}_d\end{bmatrix}\\ &+ \begin{bmatrix}\mathcal{A}_{(1,2)}\frac{\nabla\phi}{1-\phi}\cdot\nu\nabla(\overline{\mathbf{u}}_d-\overline{\mathbf{u}}_c) - \mathcal{A}_{(1,2)}\frac{\nabla^2\phi}{1-\phi}\nu(\overline{\mathbf{u}}_d-\overline{\mathbf{u}}_c)\\ \mathcal{A}_{(2,2)}\frac{\nabla\phi}{1-\phi}\cdot\nu\nabla(\overline{\mathbf{u}}_d-\overline{\mathbf{u}}_c) - \mathcal{A}_{(2,2)}\frac{\nabla^2\phi}{1-\phi}\nu(\overline{\mathbf{u}}_d-\overline{\mathbf{u}}_c)\end{bmatrix}\\ &- \begin{bmatrix}\nabla\cdot\overline{\Sigma}_{Re,d}\\ \nabla\cdot\overline{\Sigma}_{Re,c}\end{bmatrix} - \mathcal{A}\begin{bmatrix}\frac{\nabla\phi}{\phi}\cdot\overline{\Sigma}_{Re,d}\\ \frac{\nabla(1-\phi)}{1-\phi}\cdot\overline{\Sigma}_{Re,c}\end{bmatrix},\end{aligned} \tag{2}$$

where subscripts c and d indicate the continuous and dispersed (particle) phases, the overbar refers to the phase average, ϕ is the volumetric concentration of the dispersed phase, p is the pressure, ν is the kinematic viscosity of clear water, s is the specific density of the solid particle, $\mathbf{g}$ is the gravitational acceleration, Σ_{Re} is the Reynolds stress arising from variations in the sub-grid scale (SGS), τ_p is the particle relaxation time, and $\mathcal{A}$ is a partitioning matrix resulting from the added mass effect, written as

$$\mathcal{A} = \begin{bmatrix}1+\frac{C_{vm}}{s} & -\frac{C_{vm}}{s}\\ -C_{vm}\frac{\phi}{1-\phi} & 1+C_{vm}\frac{\phi}{1-\phi}\end{bmatrix}^{-1} = \frac{1}{1+\frac{C_{vm}}{s}+C_{vm}\frac{\phi}{1-\phi}}\begin{bmatrix}1+C_{vm}\frac{\phi}{1-\phi} & \frac{C_{vm}}{s}\\ C_{vm}\frac{\phi}{1-\phi} & 1+\frac{C_{vm}}{s}\end{bmatrix}. \tag{3}$$

In Eq. (2), the particle relaxation time (τ_p) is obtained according to Stokes' law as follows:

$$\tau_p = \frac{s d_p^2}{18\nu}, \tag{4}$$

where d_p is the particle diameter. An important feature of Eq. (2) with (3) is that, unlike existing equations originally formulated for solid–gas systems, the present two-phase formulation includes the effects of added mass, which are not negligible when $s = O(1)$, as in solid–liquid systems. Unlike most existing EE momentum formulations in two-phase studies on sediment suspension in which calculations are made based on the conservative quantities $\phi\overline{\mathbf{u}}_d$ and $(1-\phi)\overline{\mathbf{u}}_c$ (e.g. Greimann and Holly, 2001, 2003b,a, 2005, 2010, 2011), eliminating the dependence on ϕ in Eq. (2) ensures the well-posed grid-resolving velocity field of the dispersed phase, even when ϕ is zero. The present format, as presented in other studies on two-phase flow (e.g. Drew and Passman, 1998, 2008), is obtained through the simple manipulation of its conservative form using mass balance, which theoretically provides the same results.

The aforementioned mathematical formulations are implemented in an incompressible flow solver, which is originally developed by Zang et al. (1994) and parallelized by Cui and Street (2001) to solve the singe-phase flow problems. In this code, the finite-volume method is used to discretize the governing equations except for the convective terms, which are discretized using second-order central differences. The convective terms in the

momentum equations are discretized using a variation of QUICK (quadratic upstream interpolation for convective kinematics) (Leonard, 1979; Perng and Street, 1989) and the convective terms in the scalar transport equation are discretized using SHARP (simple high accuracy resolution program) (Leonard, 1988). This flow solver has been applied to a variety of problems related to environmental flow, such as coastal upwelling (Zang and Street, 1995; Cui and Street, 2004), rotating convective flow (Cui and Street, 2001), internal waves (Fringer and Street, 2003; Venayagamoorthy and Fringer, 2006, 2007), surface gravity wave (Hodges and Street, 1999), and sediment transport (Zedler and Street, 2001; Zedler and Street, 2006; Chou and Fringer, 2008; Chou and Fringer, 2010). The large eddy simulation in conjunction with a dynamic mixed model for the SGS turbulence closure is employed to simulate turbulent flow. Here, in order to simplify the problem and avoid additional effort in solving the closure problems in particle-laden turbulence, we neglect the Reynolds stresses and focus on the grid-resolving two-phase coupling effects.

Following Kim and Moin (1985) and Zang et al. (1994), the second-order Adams–Bashforth method is employed for the time-advancement scheme for all terms that do not associate either diffusion or the SGS model, and the Crank–Nicolson method is employed for diffusion terms. The flow solver employs the fractional-step method, in which the predicted velocity field is corrected by the projection of the pressure gradient. The pressure field is solved by enforcing zero divergence to the velocity field of the new time step, thereby resulting in a Poisson-type pressure solver with the divergence of the intermediate mixture velocity as the source. In the computation of two-phase flow, zero divergence must be applied to mixture velocity, i.e. $\nabla\cdot[\phi\overline{\mathbf{u}}_d+(1-\phi)\overline{\mathbf{u}}_c]=0$. As a result, a Poisson equation to solve the non-Boussinesq pressure is written as

$$\frac{1}{\Delta t}\nabla\cdot\left\{\begin{bmatrix}\phi^{n+1} & 1-\phi^{n+1}\end{bmatrix}\begin{bmatrix}\overline{\mathbf{u}}_d^*\\ \overline{\mathbf{u}}_c^*\end{bmatrix}\right\}=\nabla\cdot\left\{\begin{bmatrix}\phi^{n+1} & 1-\phi^{n+1}\end{bmatrix}\mathcal{A}^{n+1}\begin{bmatrix}-\frac{1}{s}\nabla\overline{p}^{n+1}\\ -\nabla\overline{p}^{n+1}\end{bmatrix}\right\}, \tag{5}$$

and the velocity at the new time step, $t=n+1$, is then corrected with

$$\begin{bmatrix}\overline{\mathbf{u}}_d^{n+1}\\ \overline{\mathbf{u}}_c^{n+1}\end{bmatrix}=\begin{bmatrix}\overline{\mathbf{u}}_d^*\\ \overline{\mathbf{u}}_c^*\end{bmatrix}+\Delta t\mathcal{A}^{n+1}\begin{bmatrix}-\frac{1}{s}\nabla\overline{p}^{n+1}\\ -\nabla\overline{p}^{n+1}\end{bmatrix}. \tag{6}$$

Thus, incompressibility is applied to the solid–liquid mixture, rather than only to the continuous phase, as in a number of previous studies (e.g. Cantero et al., 2008, 2009). As demonstrated in the following numerical examples, the effect of mixture incompressibility becomes increasingly important as particle concentration increases.

3. Numerical simulation of particle-induced Rayleigh–Taylor instability

We employ the present EE model to investigate the particle-induced RT instability and subsequent convective processes. Chou et al. (2013) presented the simple laminar case of an individual bubble. This study focuses on the case involving turbulence to examine the two-phase interaction resulting from the particle-induced RT instability, and conducted single-phase simulations for the same problem settings. This enables us to differentiate the effects of the two-phase coupling, thus determining its importance in detailed flow dynamics and vertical bulk mixing. The domain setup and results are presented in the following.

3.1. Domain setup and parameters

Simulations are carried out in a three-dimensional domain of size $L\times W\times 2H=0.08$ m $\times 0.08$ m $\times 0.12$ m, with the grid resolution given by $N_x\times N_y\times N_z=128\times 128\times 192$. The gravitational force acts along the z-direction, and the z-coordinate starts from $z=-H$ to H. Hereafter, we use the half depth H as the dimensional parameter to normalize the spatial scales. Particle diameter, $d_p=40$ μm, is used in all simulations. Each run is initialized with a sediment-containing layer in the upper half region and clear water in the lower half of the domain. Three different initial concentrations, $\phi_0=0.0032, 0.0128$, and 0.0512, are used, resulting in a total of six cases for comparison. Strictly speaking, the single phase approach is valid only for $\phi=O(0.001)$. However, in realistic problems of environmental flow, fine particle suspension can easily reach $\phi=O(0.01)$. Hence, we select a concentration of $O(0.001)$, which is within the concentration range for which single-phase approximation is valid. The case $\phi_0=0.0128$ is roughly the limit of the range, while $\phi_0=0.0512$ is far beyond the limit, showing the greatest deviation from the single-phase approximation. The interface separating the sediment-containing layer and the clear water layer is initially flat. In order to trigger the instability at the interface, flow in the sediment-containing (upper half) region is initialized with a weak, decaying homogeneous turbulence field, associated with the turbulent kinetic energy $\sqrt{u^2+v^2+w^2}=O(0.0001\ \mathrm{m^2\ s^{-2}})$. Rather than providing initial multi-mode perturbation at the interface as in most RT studies (e.g. Youngs, 1984, 1991, 2001, 2004), we initiate flow perturbation based on the idea that the sediment-containing layer must present turbulence to support suspension (Necker et al., 2002). The periodic boundary condition is applied to all horizontal boundaries, such that no lateral wall would be encountered. There is no sediment inflow flux at the top boundary, while sediment is allowed to deposit at the bottom, which results in excessive accumulation at the bottom-most cell. Particularly in two-phase simulations, this may lead to a blow-up of the simulation. Therefore, in each time step, an adjustment for the concentration in the bottom-most cell, ϕ_B, needs to be made based on simple mass balance as

$$\phi_{B,new}=\frac{\phi_B\Delta z_B+\mathbf{w}_{d,B}\phi_B\Delta t}{\Delta z_B+\frac{1}{1-pr}\mathbf{w}_{d,B}\phi_B\Delta t}=\phi_B+\frac{\frac{\mathbf{w}_{d,B}\phi_B\Delta t}{\Delta z_B}\left(1-\frac{\phi_B}{1-pr}\right)}{1+\frac{1}{1-pr}\frac{\mathbf{w}_{d,B}\phi_B\Delta t}{\Delta z_B}}, \tag{7}$$

where $\mathbf{w}_d$ is the vertical component of the dispersed-phase velocity, subscript B indicates the bottom-most cell, Δz is the height of the cell, and pr is the porosity of the depositing material and equals to 0.5 in the present study. At the bottom boundary, the condition of zero penetration is employed for the solid wall. Application of Eq. (7) is equivalent to removing the deposited sediment from the bottom-most cell.

4. Two-phase effects

Prior to the discussion of the present simulation results, it is worthwhile to summarized the two-phase effects that make the present simulation results to deviate from the single-phase approximation on the theoretical basis, which are described as follows:

1. *Non-equilibrium particle inertia (NEPI):* As the dispersed particles reach the equilibrium state, in which the gravity force balances the Stokes drag, i.e.

$$\overline{\mathbf{u}}_d=\overline{\mathbf{u}}_c-w_{s,0}\hat{\mathbf{e}}_3, \tag{8}$$

where $w_{s,0}=\tau_p g'$ is the settling velocity ($g'=g(s-1)/s$). As the deviation of particle inertia from its equilibrium state is concerned,

it was first presented in Ferry and Balachandar (2001) and also derived in the companion study (Chou et al., 2013) that in the dilute case, the velocity of the dispersed phase ($\overline{\mathbf{u}}_d$) can be written as

$$\overline{\mathbf{u}}_d = \overline{\mathbf{u}}_c - w_{s,0}\hat{\mathbf{e}}_3 + \tau_p\left(1-\frac{1}{s}\right)\frac{D\overline{\mathbf{u}}_c}{Dt}. \tag{9}$$

Therefore, it can be seen from Eq. (9) that NEPI results from the acceleration of the carrier flow.

2. *NEPI effect in the carrier flow:* It can also be shown that one can substitute Eq. (9) into the continuous-phase momentum equation of the two-phase system to obtain (Chou et al., 2013)

$$\frac{D\overline{\mathbf{u}}_c}{Dt} = \left.\frac{D\overline{\mathbf{u}}_c}{Dt}\right|_{eq} - \frac{\phi}{1-\phi}(s-1)\frac{D\overline{\mathbf{u}}_c}{Dt}, \tag{10}$$

where the first term at the RHS is the equilibrium-state (i.e Eq. (8) applies) motion of the carrier flow. It should be noted that the deviation from the equilibrium-state motion, the second term at the RHS of Eq. (10), becomes increasingly important as the particle volumetric concentration (ϕ) increases. This differs from the NEPI effect in the dispersed phase in that the latter effect is independent of the local concentration.

3. *Mixture incompressibility:* The present model ensures incompressibility of the mixture, rather than only the continuous phase. The latter case assumes that sediment particles do not occupy any volume, which is an appropriate approximation only when ϕ is very small. One can easily recognize the difference by examining the pressure Poisson solver in the computational procedure presented in Section 2. In other words, without considering the non-Boussinesq effect, Eq. (5) can be reduced to

$$\begin{aligned}\nabla^2\overline{p}^{n+1} &= \frac{1}{\Delta t}\nabla\cdot\left[\phi^{n+1}\overline{\mathbf{u}}_d^* + (1-\phi^{n+1})\overline{\mathbf{u}}_c^*\right]\\ &= \frac{1}{\Delta t}\nabla\cdot\left[\overline{\mathbf{u}}_c^* + \phi^{n+1}(\overline{\mathbf{u}}_d^* - \overline{\mathbf{u}}_c^*)\right]\\ &= \nabla^2\overline{p}_0^{n+1} - \frac{1}{\Delta t}\frac{\partial}{\partial z}(\overline{w}_{cd}\phi^{n+1}),\end{aligned} \tag{11}$$

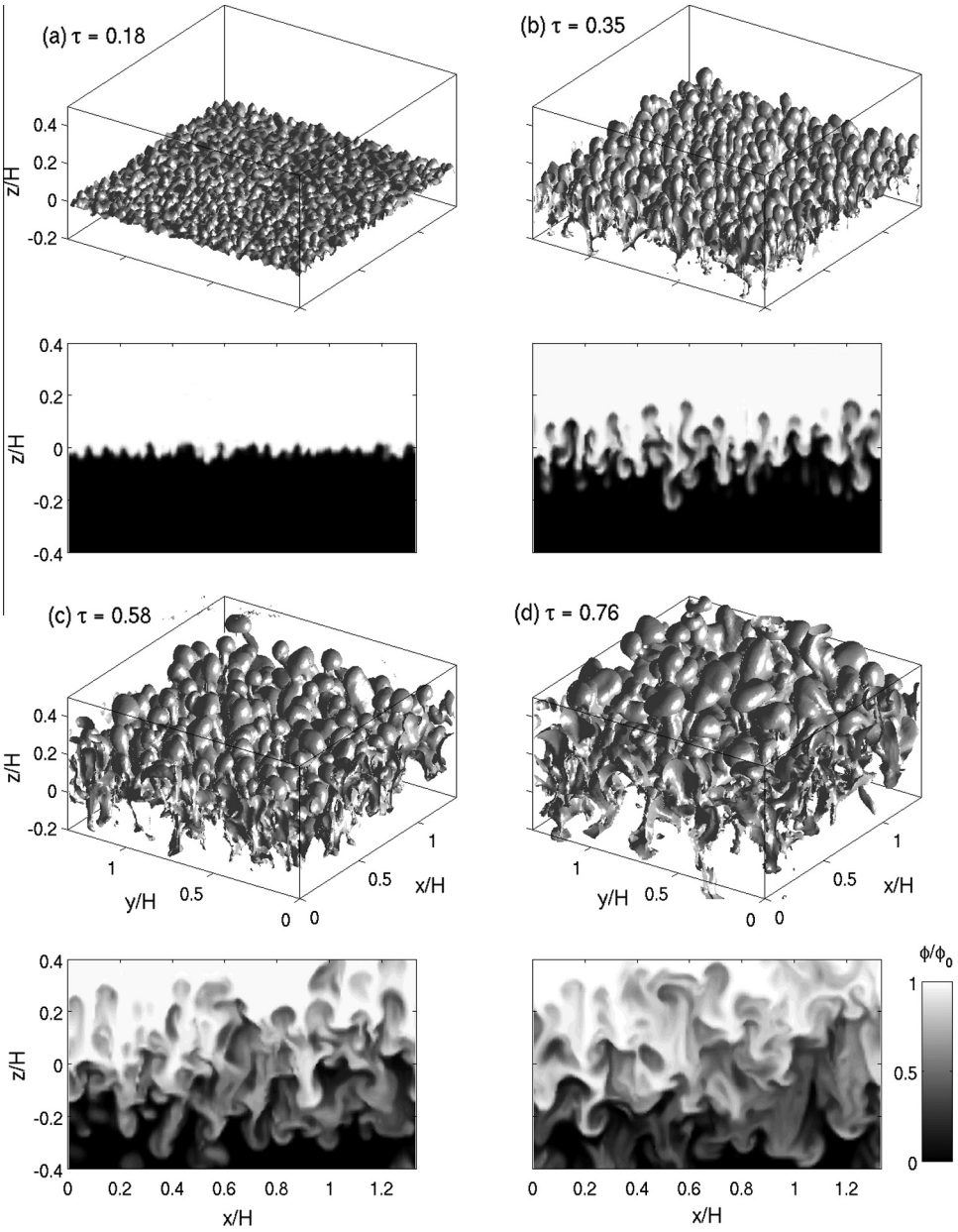

Fig. 1. Iso-surfaces of normalized concentration $\phi/\phi_0 = 0.9$ at the interface between the sediment containing layer and the clear water layer and 2-D contours at the central slice in the z-direction at four time steps in the two-phase simulation with $d_p = 40$ μm and $\phi_0 = 0.0128$.

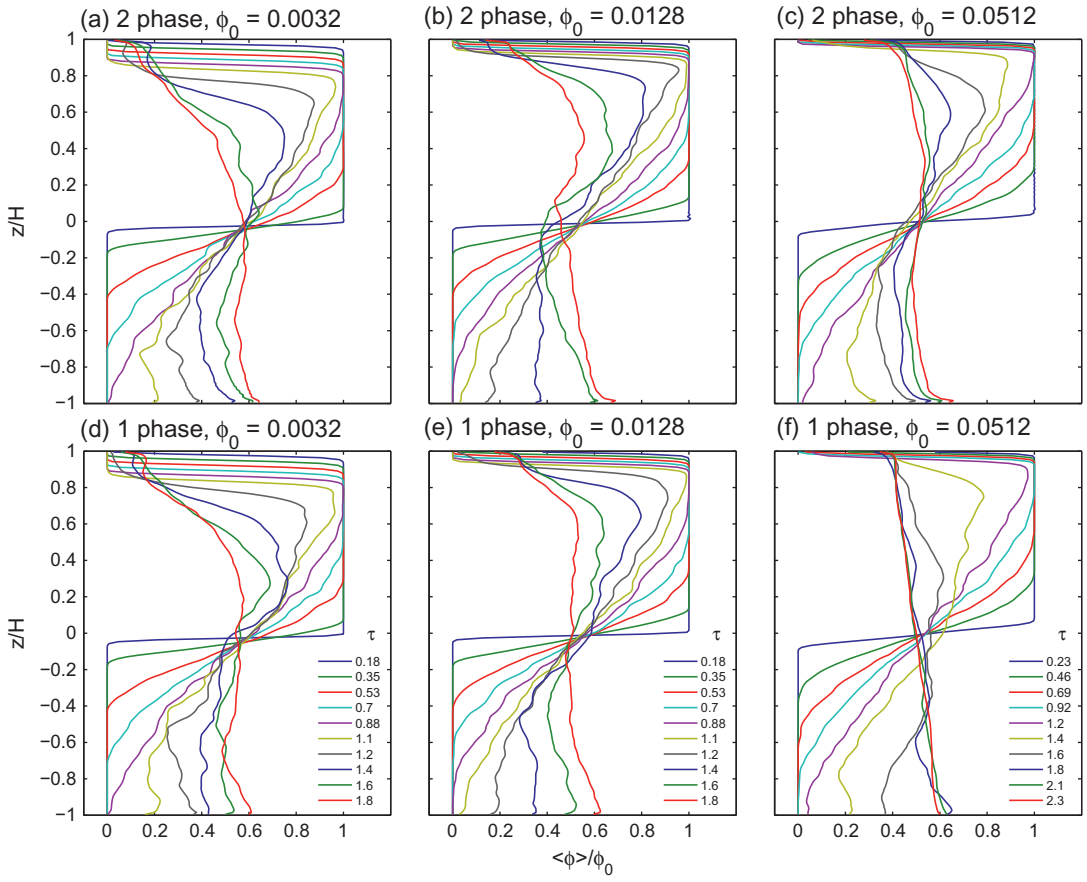

Fig. 2. Time evolutions of profiles of $\langle\phi\rangle/\phi_0$ of different ϕ_0 for $d_p = 40$ μm in (top) two-phase flow simulation and (bottom) single-phase simulation.

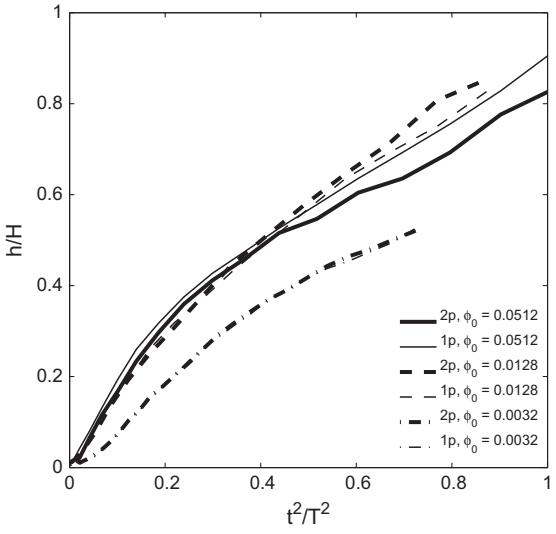

Fig. 3. Evolution of the normalized half width of the mixing zone, h_m/H, with respect to $(t/T)^2$ in two-phase and single-phase simulations with different ϕ_0.

where $\overline{p}_0^{n+1}$ is the pressure field obtained by solving the incompressibility for the continuous phase from the same predicted intermediate velocity field (denoted by the superscript $*$). Substitution of pressure obtained from Eq. (11) into the continuous- and dispersed-phase momentum equations gives an additional pressure gradient to each phase, reducing downward moving velocities.

5. Results and discussion

5.1. Instability and mixing

Snapshots of concentrations along with iso-surfaces at four representative time instants are presented in Fig. 1 to illustrate the evolution of the mixing layer. At the initial stage, irregular perturbations in the interface are triggered by the initial turbulence, as shown in Fig. 1a. Due to the randomness of the initial flow field, the initial interface perturbations are associated with a broad-band wavelength distribution $\lambda/H = 0.10 \pm 0.066$. Soon after, the amplitude grows and small-wavelength perturbations merge to form larger perturbations with $\lambda/H = 0.12 \pm 0.070$. Small flow structures continuously merge to form large plumes, exhibiting strong vertical motions (see Fig. 1c and d).

As previously mentioned, Eq. (1) has been used to describe the evolution of the mixing height as a function of time. In the present study, a consistent value $\alpha \approx 0.05$ is obtained, which is in good agreement with previous studies on the density-driven RT instability. Thus, a non-dimensional time τ is obtained by normalizing time with $T = \sqrt{H/(\alpha_0 Ag)}$ ($\alpha_0 = 0.05$), which estimates how long it takes for the mixing layer to span the half domain height. In addition, a dimensional parameter for velocity is obtained with $U = H/T$. Plotting the time evolution of profiles of horizontal averaged concentration, $\langle\phi\rangle$, enables a comparison of mixing layer growth for each case as presented in Fig. 2. In each panel of the figure, it is found that after the mixing height reaches its maximum value allowable in the domain ($\tau > 1$), the profiles tend to become uniform. During this time period, the presence of the bottom wall promotes local accumulation in near-bottom regions. Eventually,

the profiles reach a quasi-steady state and then slowly evolve with time. Because no sediment supply is provided at the top boundary, in addition to the half-depth interface that is subject to the RT instability, the other interface is found to progressively move downward from the top during the initial stage, which can be clearly seen in the case of $\phi_0 = 0.0032$ in Fig. 2.

The mixing height, h, can be obtained by measuring the half distance between $\langle\phi\rangle/\phi_0 = 0$ and 1 of the $\langle\phi\rangle$ profiles in Fig. 2. Evolution of h with respect to t^2/T^2 for different ϕ_0 before the thickness of the mixing layer reaches the domain height is plotted in Fig. 3. As $\alpha = \alpha_0$ corresponds to the diagonal straight line starting from the origin, it can be seen from Fig. 3 that α ranges from 0.4 to 0.6 in the present cases. In both single-phase and two-phase simulations, cases of $\phi_0 = 0.0032$ and 0.0128 show roughly the same growth rate of h (i.e. the same α), but the two-phase simulation with $\phi_0 = 0.0512$ shows a slower growth rate compared to the single-phase case, particularly after $t^2/T^2 > 0.45$. This is mainly caused by the NEPI effect in the continuous phase and mixture incompressibility, details of which will be discussed when flow energetics is analyzed in Section 5.3. Compared to denser cases, the case of $\phi_0 = 0.0032$ shows a relatively slow growth rate of h. The high growth rate of the mixing layer when $\phi_0 = 0.0128$ and 0.0512 can be attributed to the resulting strong turbulence, which enhances vertical mixing. In contrast, the RT instability of the most dilute case, $\phi_0 = 0.0032$, does not generate evident turbulence. The lack of strong turbulent flow field when $\phi_0 = 0.0032$ can be demonstrated from the absence of the $k^{-5/3}$ region in the energy spectrum shown in Fig. 8 for $\phi_0 = 0.0032$.

Mixing in the upper layer is dominated by the vertical motion of bubbles carrying clear low-density fluid from the lower half region. In order to obtain more insights into the dynamics of bubbles, Fig. 4 presents snapshots of the concentrations from both single-phase and two-phase simulations with different initial concentrations at the same time, $\tau = 0.94$. It can be seen that, as ϕ_0 increases (0.0128 and 0.0512), the bubble do not have geometry as well defined as in the dilute case, usually appearing with geometric irregularities, as shown in Fig. 2f. Moreover, a comparison of different ϕ_0 in Fig. 2 reveals that as ϕ_0 increases, flow is associated with structures with greater fineness. The difference between the dilute and dense cases is due to higher concentrations of sediment providing greater inter-phase drag, as it is entrained into bubbles, which in turn dampen the vertical motion more rapidly than in the dilute case. In such cases, bubbles carrying clear water soon blend with ambient turbid fluid, resulting in the rapid dissipation of bubbles. Although this enhances local mixing, as seen from the darker color of the turbid layer in the dense case compared to the dilute case in Fig. 2, the quick entrainment of sediment into bubbles reduces the bulk mixing efficiency through the suppression of vertical motion.

In addition to the inter-phase drag, the high dissipation rate of upward moving bubbles in the dense case is due to the large volume fraction of sediment that suppresses vertical motion of

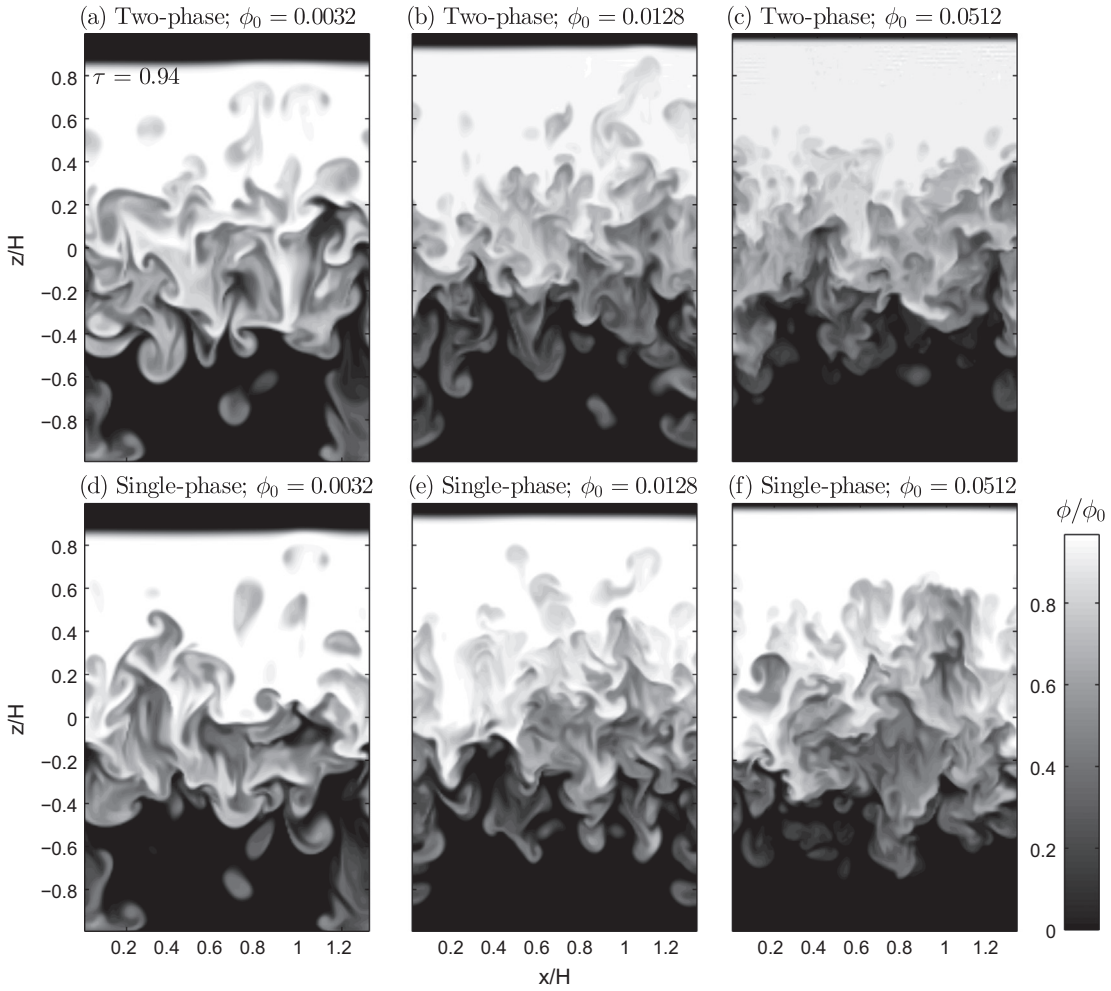

Fig. 4. Snapshots of normalized concentration contours at the central slice ($y/H = 0.67$) for all six cases at $\tau = 0.94$.

bubbles and spikes due to incompressibility of the solid–liquid mixture. This effect is critical, and in the present study, it is captured using a two-phase projection method that takes the particle volume into account. This adds additional upward pressure gradients, $\phi_0\overline{w}_{cd}$ and $\phi_0\overline{w}_{cd}/s$, to the continuous phase and dispersed phase, respectively (see Eq. (11)). This lowers the falling speed of spikes formed by the high-concentration turbid fluid, slowing down the interfacial convective process resulting from the RT instability, thereby reducing the mixing efficiency.

5.2. Excessive accumulation

The present two-phase also differs from the single-phase method with regard to additional local accumulation. It is well-known that, in dispersed two-phase systems, particles tend to segregate from regions of high vorticity and aggregate in regions of low vorticity and high strain rate. This phenomenon has been extensively studied with regard to gaseous flow (see Balachandar and Eaton, 2010 and references therein). This study focuses on accumulation in the present EE simulation in addition to the single-phase approximation induced by the NEPI and mixture incompressibility. Here, for the sake of simplicity, we assume that the major difference in velocity between two phases is the vertical component. Therefore, we introduce a quantity to measure the deviation from the equilibrium state for dispersed particles as

$$\delta\overline{w}^*_{cd} = \frac{\overline{w}_{cd} - w_{s,0}}{w_{s,0}}. \tag{12}$$

Using the relationship presented in Eq. (12), the mass balance of the dispersed phase can be written as

$$\frac{\partial\phi}{\partial t} + \nabla\cdot[(\overline{\mathbf{u}}_c - \overline{w}_{cd})\phi] = 0. \tag{13}$$

Along with the mixture incompressibility ($\nabla\cdot[\phi\overline{\mathbf{u}}_d + (1-\phi)\overline{\mathbf{u}}_c] = 0$), Eq. (13) requires a straightforward manipulation to become

$$\frac{\partial\phi}{\partial t} + \overline{\mathbf{u}}_c\nabla\phi = (1-\phi)\frac{\partial}{\partial z}(\phi\overline{w}_{cd}). \tag{14}$$

The LHS of Eq. (14) describes the movement of the passive scalar that follows the flow motion, while the RHS describes the local aggregation/segregation. Using the relationship presented in Eqs. (12), (14) can be further written as

$$\frac{D\phi}{Dt} = w_{s,0}(1-\phi)\frac{\partial}{\partial z}\phi + w_{s,0}(1-\phi)\frac{\partial}{\partial z}\left(\phi\delta\overline{w}^*_{cd}\right). \tag{15}$$

In fact, $w_{s,0}(1-\phi)$ at the RHS of Eq. (15) is the settling velocity in the equilibrium state modified by pressure coupling (see Chou et al., 2013 for detailed derivation). Therefore, the first term at the RHS of Eq. (15) is equilibrium-state accumulation. The second term at the RHS of Eq. (15) is local accumulation due to NEPI, and $1-\phi$ (appearing in both the first and second terms) is due to mixture incompressibility.

Fig. 5 presents the three-dimensional geometry of rising bubbles and the associated distribution of $\delta\overline{w}^*_{cd}$ in the case of $\phi_0 = 0.0032$. It can be seen that the bubble usually has a clearly defined mushroom-shaped geometry associated with a vortex ring. As a bubble rises in the sediment-containing water column, flow accelerates locally in the head region, while decelerating (relative to the upward velocity) within the region of the vortex ring. This leads to a negative deviation, $\delta\overline{w}^*_{cd} < 0$, in the head region and $\delta\overline{w}^*_{cd} > 0$ in the vortex region, as shown in the bottom panel of Fig. 5. As there must be a sharp increase of ϕ at the interface between the bubble and the ambient turbid fluid, Eq. (15) shows that excessive accumulation occurs in the frontal region of rising bubbles (i.e. $\partial(\phi\delta\overline{w}^*_{cd})/\partial z > 0$). In analogy to bubbles, excessive

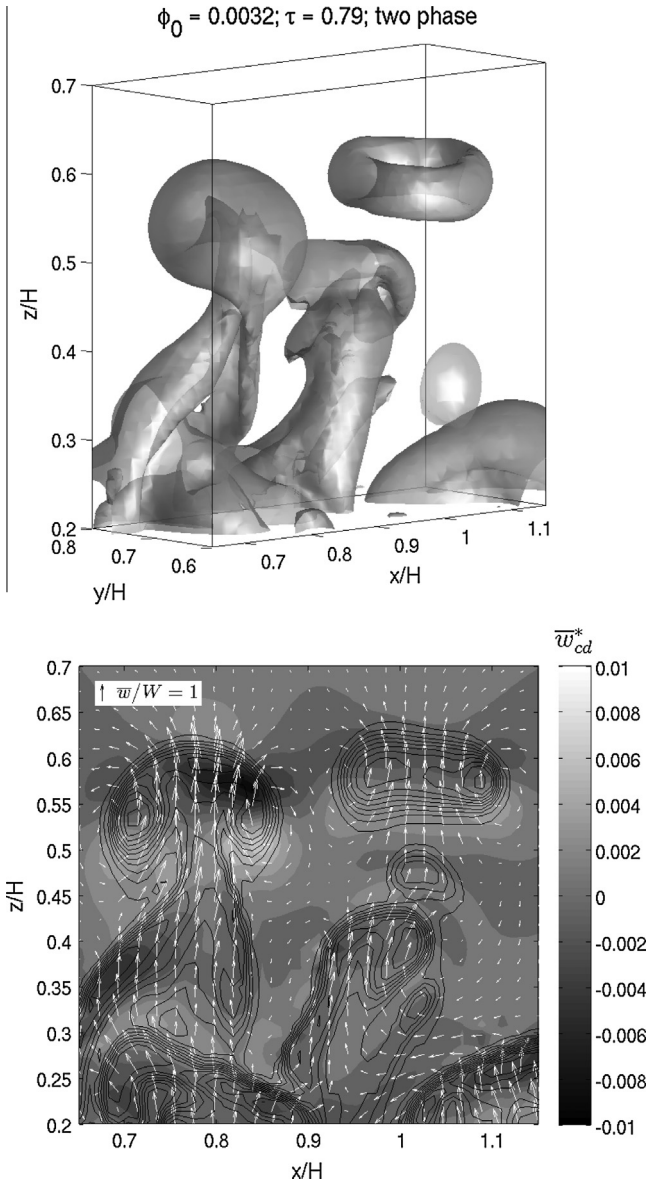

Fig. 5. Top panel: Iso-surfaces of $\phi/\phi_0 = 0.8$ in the case of $\phi_0 = 0.0032$ at $\tau = 0.79$, showing the three-dimensional geometry of rising bubbles. Bottom panel: A central slice at $y/H = 0.72$ in the top panel superimposed with normalized velocity vectors. The filled gray contours represent $\overline{w}^*_{cd}$. The concentration field is shown using black contour lines.

accumulation can also occur in the front of falling spikes. Fig. 6 presents a series of concentration and vorticity snapshots illustrating the evolution of a falling spike and the corresponding vorticity distribution. Because $\overline{w}_{cd}$ is always positive in the head region of the spike, NEPI produces additional accumulation, subsequently leading to a higher falling speed than that in the single-phase approximation. Moreover, a comparison between concentration and vorticity distribution at the later stage in Fig. 6 ($\tau \leqslant 0.81$) shows preferential accumulation along the spike, which leads to an elongated plume structure (see Fig. 6e).

5.3. Energetics

In this section, the evolution of energy budget within the computational domain is examined to elucidate the role of NEPI and mixture incompressibility in flow energetics. Here, the normalized potential energy (PE) within the domain is calculated with

$$PE = \frac{1}{PE_0}\int_{-H}^{H}\int_{0}^{W}\int_{0}^{L}(\rho_s - \rho_0)gzdxdydz, \quad (16)$$

where PE_0 is the initial potential energy. In the two-phase case, the normalized vertical kinetic energy, K_z is calculated with

$$K_z = \frac{1}{PE_0}\int_{-H}^{H}\int_{0}^{W}\int_{0}^{L}\rho_s\phi\overline{w}_d^2 + \rho_0(1-\phi)\overline{w}_c^2 dxdydz, \quad (17)$$

while in the single-phase approach, we replace $\overline{w}_c$ with $\overline{w}$ and $\overline{w}_d$ with $\overline{w}_c + w_{s,0}$. Normalized horizontal kinetic energy, K_{xy}, is calculated with

$$K_{xy} = \frac{1}{PE_0}\int_{-H}^{H}\int_{0}^{W}\int_{0}^{L}\rho_s\phi(\overline{u}_d^2 + \overline{v}_d^2) + \rho_0(1-\phi)(\overline{u}_c^2 + \overline{v}_c^2)dxdydz \quad (18)$$

in two-phase simulations, and $\overline{u}_c = \overline{u}_d = \overline{u}$ and $\overline{v}_c = \overline{v}_d = \overline{v}$ in Eq. (18) for single-phase simulation. Fig. 7 presents the time evolution of the release of normalized potential energy, $\Delta PE = 1 - PE$, and kinetic energy in all cases. Generally, because flow motion is initially dominated by vertical motion associated with bubbles and spikes, the vertical kinetic energy, K_y first reaches its peak value before the peak of the horizontal kinetic energy K_{xy}. The total kinetic energy, K, reaches a maximum when $\tau \approx 1.65$, the point at which mixing nears completion, i.e. concentration profiles in Fig. 2 become uniform. It can bee seen in Fig. 7a and b that as long as the initial suspension is not exceedingly dense, an increase in initial concentration increases the amount of potential energy that is transformed into kinetic energy. The transfer rate $(K/\Delta PE)$ at the time corresponding to the occurrence of the maximum kinetic energy is 0.21 when $\phi_0 = 0.0032$ and 0.36 when $\phi_0 = 0.0128$.

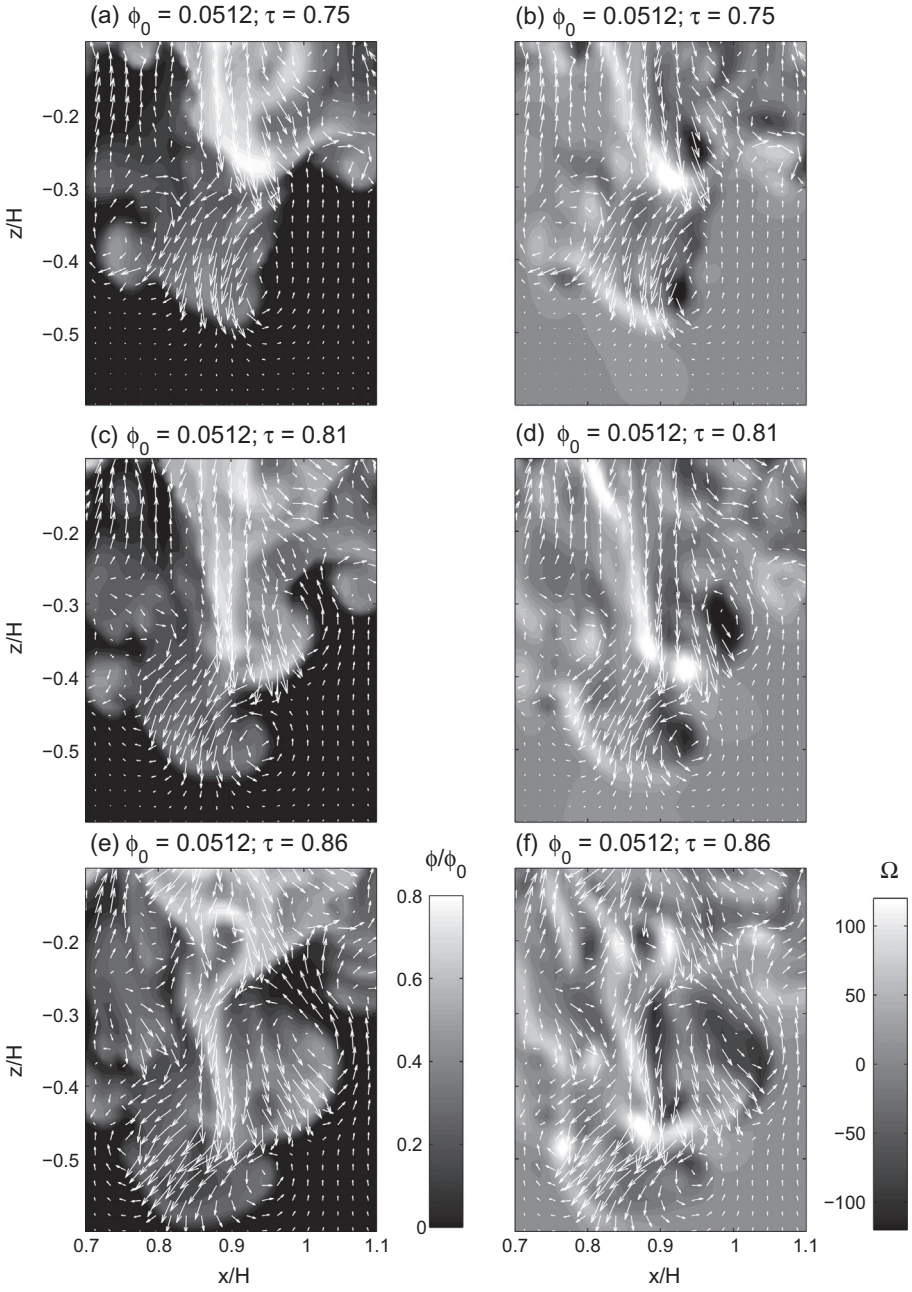

Fig. 6. Snapshots of normalized sediment concentration (left column) at the middle x,z-transect $(y/H = 0.67)$ of a falling spike superimposed with velocity vectors at $\tau = 0.075$ (top), 0.81 (middle), and 0.86 (bottom) and corresponding distributions of the normalized vorticity (Ω) (right column).

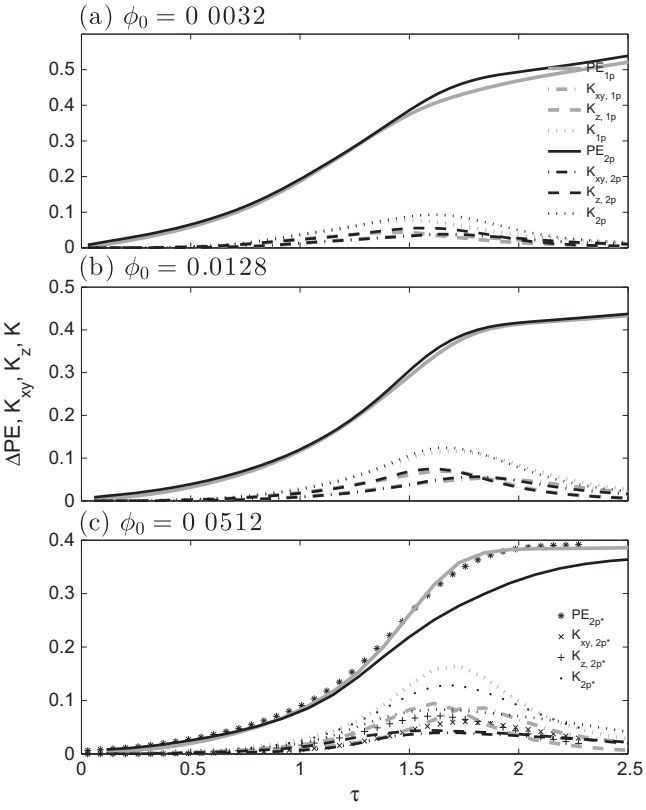

Fig. 7. Time evolutions of the release of potential energy ($\Delta PE = 1 - PE$) and kinetic energy (K_{xy}, K_z, and $K = K_{xy} + K_z$) for (a)$\phi_0 = 0.0032$, (b) $\phi_0 = 0.0128$, and (c) $\phi = 0.0512$. The representation of each line is outlined in the legend in (a), in which subscripts $2p$ and $1p$ indicate two-phase and single-phase simulations, respectively. In (c), the results are obtained from two-phase simulation without considering mixture incompressibility ($\nabla \cdot \overline{\mathbf{u}}_c$), as indicated by the subscript $2p^*$ in the legend.

The comparison in Fig. 7a shows the appreciably larger value of K in the two-phase flow simulation, which is due to NEPI. Because NEPI is not a function of local concentrations, the resulting enhancement of vertical motion of the dispersed phase in the two-phase simulation is significant in dilute suspensions, corresponding to vertical mixing of a greater efficiency. As the initial concentration increases ($\phi_0 = 0.0128$), the NEPI effect in the continuous phase and mixture incompressibility become more important. These two effects suppress vertical motion of the mixture such that, combined with NEPI of the dispersed phase, no significant deviation is found between single-phase and two-phase results, as shown in Fig. 7b. As the initial concentration becomes increasingly dense ($\phi_0 = 0.0512$), vertical motion is strongly suppressed by the additional pressure gradient resulting from mixture incompressibility. As shown in Fig. 7c, this corresponds to a significant reduction in the time evolution of ΔPE as well as a lower K. Fig. 7c also plots data points from the two-phase simulation that does not take mixture incompressibility into account (indicated by the subscript $2p^*$). A comparison of these results with those of single-phase simulation illustrates that, although time evolutions of ΔPE are very similar, a significant reduction of kinetic energy can be caused by the NEPI effect in the continuous phase in the dense suspension. Moreover, a comparison with the present two-phase case (in which mixture compressibility is considered) shows that the potential energy releases in a significantly slower rate due to mixture incompressibility. This demonstrates the importance of mixture incompressibility in bulk mixing behavior in dense suspensions.

As a quantitative measurement of the transfer rate for dense suspensions in the present simulations (Fig. 7c), the single-phase simulation shows a high transfer rate with $K/\Delta PE = 0.46$, while the two phase simulation without mixture incompressibility gives 0.39, at the same time that K reaches its maximum value. Taking mixture incompressibility into account results in a reduction in the transfer rate to 0.33 and induces a significant reduction in the release of potential energy, such that the peak in kinetic energy is only approximately 50% of the value obtained from the single-phase simulation. This demonstrates that a significant proportion of the energy dissipation can be attributed to the suppression of bubble motion by mixture incompressibility.

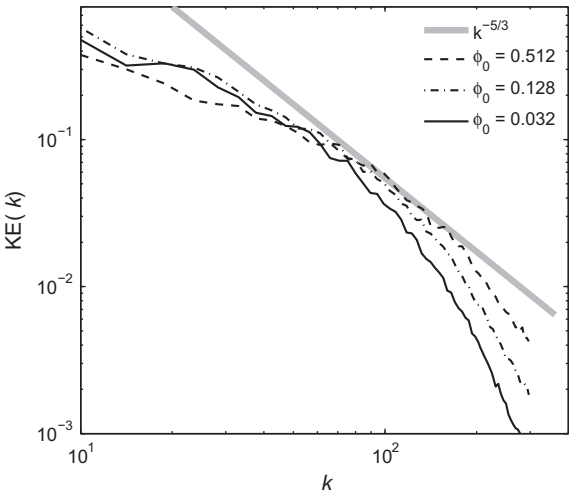

Fig. 8. Spectra of the kinetic energy from the two-phase simulation at the middle plane in the vertical direction ($z = 0$) for three initial concentrations at the time corresponding to the occurrence of the maximum kinetic energy in Fig. 7.

We further examine flow turbulence. The spectra of the turbulent kinetic energy (TKE) of the middle plan ($z/H = 0$) in the vertical direction are plotted in Fig. 8 for different ϕ_0 in two-phase flow simulations. The instantaneous TKE data are measured at the same time that the peak kinetic energy reaches its maximum value, as presented in Fig. 7. Thus, these can be examined under conditions of the greatest turbulence intensity in each case. As shown in Fig. 8, in the case of $\phi_0 = 0.0512$ and 0.0128, there is a fully developed turbulence field, corresponding a range of energy spectrum with slope = $-5/3$. In the case of $\phi_0 = 0.0512$, this ranges roughly from the normalized wave number k ($= 2\pi H/\lambda$)= 60–160 while in the case of $\phi_0 = 0.0128$, it ranges from $k = 70$ to 120. However, in the case when $\phi_0 = 0.0032$, no strong evidence is obtained to indicate the development of turbulence, leading to the conclusion that the flow is fairly laminar. This can be observed in the snapshot of the concentration field in Fig. 4, which shows larger-scale variations in concentration without small-scale fluctuations as in the cases of the denser suspension. Moreover, compared to the dense cases, the dilute case of Fig. 4a and 4d presents a more pronounced contrast in concentration contrast of bubbles/spikes to ambient colors, indicating that the entrainment from the ambient flow is far lower in the dilute case due to the low intensity of flow turbulence.

6. Summary and conclusion

This paper presents a two-way coupled EE numerical model to simulate the suspension of fine particles in liquid. In addition to inter-phase drag, the present numerical model allows for more complete consideration of solid–fluid interactions, namely added mass and mixture incompressibility. Added mass is taken into account via the inversion of a matrix obtained from the theoretical derivation. The mathematical formulation is discretized on a

finite-volume framework, and mixture incompressibility is ensured using a two-phase pressure projection method that solves the non-Boussinesq pressure field.

The numerical model is then applied to investigate the particle-driven RT instability and the resulting large-scale vertical convection of fine sediment ($d_p = 40$ μm) in a simple three-dimensional setting. The simulation results show that the parameter, α, which indicates the growth rate of the mixing layer of the RT instability, ranges from 0.04 to 0.06 in all cases. These are in strong agreement with those reported in previous studies. It is also found that when the initial concentration, ϕ_0, is dilute, additional momentum components of the dispersed phase resulting from NEPI slightly increase the efficiency of vertical mixing. As ϕ_0 increases, the NEPI feedback to the continuous phase and the influence of mixture incompressibility become increasingly important. In particular, mixture incompressibility exerts an additional upward pressure gradient, which suppresses downward motion of high-density fluid, thereby reducing interfacial mixing associated with the RT instability. This is significant in the densest case ($\phi_0 = 0.0512$). In addition, we present the theoretical basis to describe excessive accumulation due to NEPI and mixture incompressibility. The spatial distribution of the deviation from the Stokes settling velocity for the dispersed phase shows that excessive accumulation occurs in frontal areas of both bubbles and spikes.

The study also analyzes flow energetics. When the initial concentration is dilute (e.g. $\phi_0 = 0.0032$), the time evolutions of the energy budget shows that the transformation rate from the release of potential energy to kinetic energy is approximately 0.2, which increases with an increase in initial concentration (e.g. 0.36 when $\phi_0 = 0.0128$). However, this trend only holds under dilute conditions. With a denser initial concentration (such as $\phi_0 = 0.0512$), mixture incompressibility results in a considerable reduction of the release of potential energy and its transformation to kinetic energy. Moreover, plots of the flow energy spectrum at the middle plane in the vertical direction at the time corresponding to the highest kinetic energy for each case show the broadest spectrum of the homogeneous turbulence regime (slope $= -5/3$) in the case of $\phi_0 = 0.0512$, while in the case of greatest dilution, the flow is not associated with evident turbulence.

In conclusion, the present three-dimensional numerical model provides a comprehensive consideration of particle–fluid interaction for problems related to fine suspension. Our results have critical implications for the single-phase modeling of sediment suspension problems. Despite the fact that the single-phase approximation remains an appealing approach without the requirement of using the the infinitesimal computational time step ($< \tau_p$), the underlying assumption prevents it from capturing NEPI, which is accessible only via the two-phase method. However, mixture incompressibility can be included by modifying the source term to include the sediment flux to solve the pressure field in the incompressible flow solver. According to the findings of the present study, this provides far greater accuracy, particularly when concentrations are dense.

Acknowledgements

The authors gratefully acknowledge the support of Taiwan NSC Civil and Hydraulic Engineering Program under Grant 101-2218-E-002-004. The research assistantship of W.R.S. was supported by the NSC fund (100-2627-B-002-008) Granted to F.C.W. Y.J.C. thanks Oliver Fringer at Stanford University for his extensive suggestions for the development of the present numerical model. The computation is performed on the Dell PowerEdge M620 supercomputer cluster located at Taida Institute of Mathematical Science (TIMS) at National Taiwan University, which is gratefully acknowleged.

References

Amoudry, L., Hsu, T.-J., Liu, L.-F., 2005. Two-phase model for sand transport in sheet flow regime. J. Geophys. Res. 110, C09003.
Balachandar, S., Eaton, J.K., 2010. Turbulent dipersed multiphase flow. Ann. Rev. Fluid Mech. 42, 111–133.
Bradley, W.H., 1965. Vertical density currents. Science 150, 1423–1428.
Burns, P., Meiburg, E., 2012. Sediment-laden fresh water above salt water: linear stability analysis. J. Fluid Mech. 691, 279–314.
Cantero, M.I., Balachandar, S., Garcia, M.H., 2008. An Eulerian–Eulerian model for gravity currents driven by intertial particles. Int. J. Multiphase Flow 34, 484–501.
Cantero, M., Balachandar, S., Cantelli, A., Pirmez, C., Parker, G., 2009a. Turbidity current with a roof: direct numeriacl simulation of self-stratified turbulent channel flow driven by suspended sediment. J. Geophys. Res. 114, C03008.
Cantero, M., Balachandar, S., Parker, G., 2009b. Direct numerical simulation of stratification effects in a sediment-laden turbulent channel flow. J. Turbul. 10, 1–28.
Chen, X., Li, Y., Niu, X., Li, M., Chen, D., Yu, X., 2011. A general two-phase turbulent flow model applied to the study of sediment transport in open channels. Int. J. Multiphase Flow 37, 1099–1108.
Chou, Y.J., Fringer, O.B., 2008. Modeling dilute sediment suspension using large-eddy simulation with a dynamic mixed model. Phys. Fluids 20, 11503.
Chou, Y.-J., Wu, F.-C., Shih, W.-R., 2014. Toward numerical modeling of fine particle suspension using a two-way coupled Euler–Euler model: Part 1: formualtion and comparison to single-phase approximation. Int. J. Multiphase Flow 64, 35–43.
Chou, Y.J., Fringer, O.B., 2010. A model for the simulation of coupled flow-bed form evolution in turbulent flows. J. Geophys. Res: Oceans (1978–2012) 115.
Cui, A., Street, R.L., 2001. Large-eddy simulation of turbulent rotating convective flow development. J. Fluid Mech. 447, 53–84.
Cui, A., Street, R.L., 2004. Large-eddy simulation of coastal upwelling flow. Environ. Fluid Mech. 4, 197–223.
Dimonte, G., Youngs, D.L., Dimits, A., Weber, S., Marinak, M., 2004. A comparative study of the turbulent Rayleigh–Taylor instability uisng high-resolution three-dimensional numerical simulations: the Alpha-Group collaboration. Phys. Fluids 16, 1668–1693.
Drew, D.A., Passman, S.L., 1998. Theory of Multicomonent Fluids. Springer-Verlag, New York.
Ferry, J., Balachandar, S., 2001. A fast Eulerian method for disperse two-phase flow. Int. J. Multiphase Flow 27, 1199–1226.
Fringer, O.B., Street, R.L., 2003. The dynamics of breaking progressive interfacial waves. J. Fluid Mech. 494, 319.
Greimann, B.P., Holly Jr., F.M., 2001. Two-phase flow analysis of concentration profiles. J. Hydraul. Eng. 127, 753.
Hodges, B.R., Street, R.L., 1999. On simulation of turbulent nonlinear free-surface flows. J. Comput. Phys. 151, 425–457.
Hoyal, D.C., Bursik, M.I., Atkinson, J.F., 1999. Settling-driven convection: a mechanism of sedimentation from stratified fluids. J. Geophys. Res. 104, 7953–7966.
Hsu, T.-J., Jenkins, J.T., Liu, L.-F., 2003a. On two-phase sediment transport: sheet flow of massive particles. Proc. Roy. Soc. A 460, 2223–2250.
Hsu, T.-J., Jenkins, J.T., Liu, L.-F., 2003b. On two-phase sediment transport: dilute flow. J. Geophys. Res. 108, 3057.
Jha, S.K., Bombardelli, F.A., 2010. Toward two-way flow modeling of nondilute sediment transport in open channels. J. Geophys. Res. 115, F03015.
Kim, J., Moin, P., 1985. Application of a fractional-step method to incompressible Navier–Stokes equations. J. Comput. Phys. 59, 308–323.
Leonard, B.P., 1979. A stable and accurate convective modelling procedure based on quadratic upstream interpolation. Comput. Methods Appl. Mech. Eng. 19, 59.
Leonard, B.P., 1988. Simple high-accuracy resolution program for convective modelling of discontinuities. Int. J. Num. Methods Fluids 8, 1291.
Linden, P.F., Redondo, J.M., Youngs, D.L., 1994. Molecular mixing in Raylegigh–Taylor instabilities. J. Fluid Mech. 265, 97–124.
Maxworthy, T., 1999. The dynamics of sedimenting surface graviry currents. J. Fluid Mech. 392, 27–44.
Necker, F., Hartel, C., Kleiser, L., Meiburg, E., 2002. High-resolution simulations of particle-driven gravity currents. Int. J. Multiphase Flow 28, 279–300.
Necker, F., Hartel, C., Kleiser, L., Meiburg, E., 2006. Mixing and dissipation in particle-driven gravity currents. J. Fluid Mech. 545, 339–372.
Parsons, J.D., Bush, J.W.M., Syvitski, J.P.M., 2001. Hyperpycnal plume formation from riverine outflows with small sediment concentrations. Sedimentology 48, 465–478.
Perng, C.Y., Street, R.L., 1989. 3-D unsteady flow simulation: alternative strategies for a volume-average calculation. Int. J. Numeric. in Fluids 6, 927.
Read, K.I., 1984. Experimental investigation of turbulent mixing by Rayleigh–Taylor instability. Physica D 12, 45–58.
Riber, E., Moureau, V., Garcia, M., Poinsot, T., Simonin, O., 2009. Evaluation of numerical strategies for large eddy simulation of particulate two-phase recirculating flows. J. Comput. Phys. 228, 539–564.
Shringarpure, M., Cantero, M.I., Balachandar, S., 2012. Dynamics of complete turbulence suppression in turbidity currents driven by monodisperse suspensions of sediment. J. Fluid Mech. 712, 384–417.
Venayagamoorthy, S.K., Fringer, O.B., 2006. Numerical simulations of the interaciton of internal waves with a shelf break. Phys. Fluids 18, 076603.

Venayagamoorthy, S.K., Fringer, O.B., 2007. On the formation and propagation of nonlinear internal boluses across a shelf break. J. Fluid Mech. 577, 137–159.
Young, Y., Tufo, H., Dubey, A., Rosner, R., 2001. On the miscible Rayleigh–Taylor instablility two and three dimensions. J. Fluid Mech. 447, 377–408.
Youngs, D.L., 1984. Numerical simulaiton of turbulent mixing by Rayleigh–Taylor instablility. Physica D 12, 32–44.
Youngs, D.L., 1991. Three-dimensional numerical simulaiton of turbulent mixing by Rayleigh–Taylor instablility. Phys. Fluids A 3, 1312–1320.
Zang, Y., Street, R.L., 1995. Numerical simulation of coastal upwelling and interfacial instability of a rotational and stratified fluid. J. Fluid Mech. 305, 47.
Zang, Y., Street, R.L., Koseff, J.R., 1994. A non-staggered grid, fractional step method for time-dependent incompressible Navier–Stokes equations in curvilinear coordinates. J. Comput. Phys. 114, 18.
Zedler, E.A., Street, R.L., 2001. Large-eddy simulation of sediment transport: current over ripples. J. Hydraul. Eng. 127, 444.
Zedler, E.A., Street, R.L., 2006. Sediment transport over ripples in oscillatory flow. J. Hydraul. Eng. 132, 1.